

First results on the cluster galaxy population from the Subaru Hyper Suprime-Cam survey. I. The role of group or cluster environment in star formation quenching from $z = 0.2$ to 1.1

Hung-Yu Jian^{1*}, Lihwai Lin¹, Masamune Oguri^{2,3,4}, Atsushi Nishizawa⁵, Masahiro Takada⁴, Surhud More⁴, Yusei Koyama^{6,7}, Masayuki Tanaka⁸, Yutaka KOMIYAMA^{8,9}

¹Institute of Astronomy & Astrophysics, Academia Sinica, 106, Taipei, Taiwan, R.O.C.

²Research Center for the Early Universe, University of Tokyo, Tokyo 113-0033, Japan

³Department of Physics, University of Tokyo, Tokyo 113-0033, Japan

⁴Kavli Institute for the Physics and Mathematics of the Universe (Kavli IPMU, WPI), University of Tokyo, Chiba 277-8582, Japan

⁵Institute for Advanced Study, Nagoya University, Furocho Chikusaku Nagoya 4648602, Aichi, Japan

⁶Department of Astronomical Science, SOKENDAI, Osawa, Mitaka, Tokyo 181-8588, Japan

⁷Subaru Telescope, National Astronomical Observatory of Japan, 650 North Aohoku Place, Hilo, HI 96720, USA

⁸National Astronomical Observatory of Japan, Osawa 2-21-1, Mitaka, Tokyo 181-8588, Japan

⁹The Graduate University for Advanced Studies, 2-21-1 Osawa, Mitaka, Tokyo 181-8588, Japan

*E-mail: hyjian@asiaa.sinica.edu.tw

Received (reception date); Accepted (acceptation date)

Abstract

We utilize the HSC CAMIRA cluster catalog and the photo- z galaxy catalog constructed in the HSC wide field (S16A), covering $\sim 174 \text{ deg}^2$, to study the star formation activity of galaxies in different environments over $0.2 < z < 1.1$. We probe galaxies down to $i \sim 26$, corresponding to a stellar mass limit of $\log_{10}(M_*/M_\odot) \sim 8.2$ and ~ 8.6 for star-forming and quiescent populations, respectively, at $z \sim 0.2$. The existence of the red sequence for low stellar mass galaxies in clusters suggests that the environmental quenching persists to halt the star formation in the low-mass regime. In addition, star-forming galaxies in groups or clusters are systematically biased toward lower values of specific star formation rate by 0.1 – 0.3 dex with respect to those in the field and the offsets shows no strong redshift evolution over our redshift range, implying a universal slow quenching mechanism acting in the dense environments since $z \sim 1.1$. Moreover, the environmental quenching dominates the mass quenching in low mass galaxies, and the quenching dominance reverses in high mass ones. The transition mass is greater in clusters than in groups, indicating that the environmental quenching is more effective for massive galaxies in clusters compared to groups.

Key words: galaxies: clusters: general — galaxies: groups: general — large-scale structure of universe

— methods: data analysis

1 Introduction

It is well established that clusters at $z < 1$ are dominated by galaxies with redder colors, older stellar populations, early type morphologies, and little star formation, as opposed to the field environments. Many scenarios related to cluster environments have been proposed to explain how the star formation is ceased in clusters, including processes, such as ram-pressure stripping (Gunn & Gott 1972; Dressler & Gunn 1983), and galaxy-galaxy interaction (Mihos & Hernquist 1994) that quench star formation over a short timescale, and ‘strangulation’, referring to the removal of warm and hot gas (Larson et al. 1980; Balogh et al. 2000), which slowly reduces the cold gas supply. Studying the quenching timescale for cluster galaxies hence provides a powerful way to constrain the physical mechanisms responsible for the star formation quenching.

One of the tools to constrain the quenching timescale is the comparison of the properties of star-forming galaxies between different environments. It is found that star-forming galaxies (hereafter, SF population) form a tight sequence on the SFR and stellar mass plane, the so-called ‘main sequence’ (Brinchmann et al. 2004; Noeske et al. 2007; Elbaz et al. 2007; Daddi et al. 2007; Pannella et al. 2009; Magdis et al. 2010; Lin et al. 2012; Whitaker et al. 2012; Heinis et al. 2014). It is expected that slow quenching would lead to an overall reduction of the specific star formation rates (sSFRs) of the SF population whereas a fast quenching mainly changes the fraction of quenched population without altering the sSFR of the remaining SF galaxies. Previous studies have suggested that the difference in the star formation activities between the field and the cluster environments is primarily driven by the relative red fraction, instead of the properties of the SF population (Muzzin et al. 2012; Koyama et al. 2013; Lin et al. 2014; Wagner et al. 2017; Jian et al. 2017). Using Pan-STARRS1 clusters (Lin et al. 2014; Jian et al. 2017), it is found that the specific star formation rates (sSFRs) of SF galaxies in the clusters are only moderately lower than those the field (< 0.2 - 0.3 dex) and the difference becomes insignificant on groups scales. However, the uncertainty remains large for high mass galaxies because of the small sample sizes used in these studies, and it is also uncertain that the environmental quenching can extend to low mass galaxies.

In this work, we probe the properties of cluster galaxies using a large sample drawn from the HSC Subaru Strategic Program (hereafter the HSC survey). The HSC survey (Aihara et al. 2017) consists of three survey layers, ‘Wide’, ‘Deep’, and ‘UltraDeep’ components. The cluster sample used in this work comes from the HSC CAMIRA (Cluster finding Algorithm based on Multi-band Identification of Red-sequence gAlaxies) catalog (Oguri et al. 2017) constructed in the HSC Wide

field, reaching $i \sim 26$ at 5σ over 174 deg^2 . It contains 4972 clusters with richness larger than 10 in the redshift range of $0.2 < z < 1.1$. This allows us not only to extend the analysis to redshifts greater than 0.8 and to fainter galaxy populations by 2 magnitudes in i , but also to increase the sample size by a factor of 17 compared to our previous works (Lin et al. 2014; Jian et al. 2017). There are two other companion papers in this special issue to address the environmental effects but using different catalogs and methods. Koyama et al. (2017) make use of the NB emitter catalogs constructed for HSC-SSP Deep and UltraDeep fields to search for “red emitter” along the large-scale structures at $0.2 < z < 1.7$ and identify their environments. Nishizawa et al. (2017) utilize the CAMIRA catalog to study the evolution of cluster profile for red and blue populations out to $z < 1.1$ and reveal the color-magnitude relation of red-sequence galaxies at the faint end $z < 24$.

Our paper is formatted as follows. In Section 2, we briefly describe the data, the sample selection, and the analysis method. In Section 3, we present the main results, discussing the main sequence properties, and the redshift and mass dependence of field, group, and cluster galaxy properties. In Section 4, our conclusion and discussion are presented. Throughout this paper we adopt the following cosmology: Throughout this paper we adopt the following cosmology: $H_0 = 100h \text{ km s}^{-1} \text{ Mpc}^{-1}$, $\Omega_m = 0.3$ and $\Omega_\Lambda = 0.7$. We adopt the Hubble constant $h = 0.7$ when calculating rest-frame magnitudes. All magnitudes are given in the AB system.

2 Data, Sample Selection, and Method

2.1 HSC Galaxy Sample

Hyper Suprime-Cam (HSC) Survey is conducted as part of a 300-night Strategic Survey Program (SSP) over 5 years starting from March of 2014, aiming to explore the nature of dark matter and dark energy as well as the evolution of galaxies. The first public data of HSC-SSP are released recently (Aihara et al. 2017). The Survey utilizes the wide field of view of 1.77 square degrees of Hyper Suprime-Cam to collect broad-band images in *grizy* bands as well as to study emission line objects at high redshifts through a number of narrow-band filters (Aihara et al. 2017). HSC Survey consists of a three-layered imaging, including Wide, Deep, and UltraDeep. The aimed coverage for the Wide survey has $1,400$ square degrees of the sky in all the five broad-band filters located around the equator and two large stripes around the spring and autumn equator with an additional stripe around the Hectomap region. The Deep survey is carried out in four separate fields; XMM-LSS, Extended-COSMOS (ECOSMOS), ELAIS-N1 and DEEP2-F3,

and the UltraDeep has two fields, COSMOS and SXDS. The detail survey description can be found in Aihara et al. (2017).

In this study, we make use of the S16A photometric redshift catalog based on the S16A internal data release of the HSC Survey released in 2016 August. The HSC Wide S16A dataset contains imaging data taken between 2014 March and 2016 April in all five broad-bands at full depth and covers $\sim 174 \text{ deg}^2$. The HSC data is processed by the HSC Pipeline, or hscPipe (Bosch et al. 2017, in prep.), which is based on the Large Synoptic Survey Telescope pipeline (Ivezic et al. 2008; Axelrod et al. 2010; Jurić et al. 2015). In addition, the HSC astrometry and photometry are calibrated against the Pan-STARRS1 3π catalog (Tonry et al. 2012; Schlafly et al. 2012; Magnier et al. 2013). For more detail descriptions, readers are referred to Aihara et al. (2017).

2.2 CAMIRA Groups/Clusters

The group/cluster sample is a product produced by a cluster-finding algorithm CAMIRA (Cluster finding algorithm based on Multi-band Identification of Red sequence gAlaxies) as described in Oguri (2014). Based on the stellar population synthesis (SPS) model of Bruzual & Charlot (2003), CAMIRA fits all photometric galaxies for an arbitrary set of bandpass filters and computes likelihoods of being red-sequence galaxies as a function of redshift. To improve the accuracy of the model prediction, additional calibration is done through using a sample of spectroscopic galaxies to derive residual colors of SPS model fitting as a function of wavelength and redshift. The detailed methodology of the CAMIRA algorithm can be found in Oguri (2014).

In this work, we utilize a new optically selected CAMIRA cluster catalog from the first two years of observation of the HSC Survey, i.e. the HSC Wide S16A CAMIRA catalog (Oguri et al. 2017), to study galaxies properties in groups and clusters. The sample contains 4972 clusters/groups with richness $N_{mem} > 10$ in redshift range of $0.1 < z < 1.1$, and is validated through comparisons with spectroscopic and X-ray data as well as mock galaxy catalogs. It is shown in Oguri et al. (2017) that the redshift evolution of the mass threshold is not strong. That is, the constant richness cut roughly corresponds to the constant halo mass cut. Based on the cluster redshifts and the richness N_{mem} , we bin the clusters into three redshift ranges, $0.2 < z < 0.5$, $0.5 < z < 0.8$, and $0.8 < z < 1.1$, to study their evolution and two richness ranges, $10 < N_{mem} < 25$ and $N_{mem} > 25$, to explore the “group” and “cluster” environment, respectively. Here $N_{mem} = 10$ and 25 correspond to the virial halo mass $\log_{10}(M_{vir}/h^{-1} M_{\odot}) \sim 13.61 \pm 0.13$ and 14.19 ± 0.02 , based on Equation 40 in Oguri (2014). Be noted that clusters with richness less than 15 are not included in Oguri et al. (2017) since these less massive clusters (or groups) suffer more

Table 1. CAMIRA Cluster Catalog

Redshift	z_{median}	Group	Cluster
		$10 < N_{mem} < 25$ $M_{vir}/M_{\odot} = 10^{13.6-14.2}$	$N_{mem} > 25$ $10^{>14.2}$
$0.2 < z < 0.5$	0.33	1139	194
$0.5 < z < 0.8$	0.68	1506	153
$0.8 < z < 1.1$	0.92	1611	95

contamination.

2.3 The photo-z catalog and stellar mass estimation

Photometric redshifts and physical properties of galaxies such as stellar mass and star formation rate are inferred using a photometric redshift code Mizuki (Tanaka 2015). It is a template fitting code and templates are generated using Bruzual & Charlot (2003). When deriving stellar masses and star formation rates, the Chabrier initial mass function (IMF) is assumed (Chabrier 2003). The code applies a set of Bayesian priors on physical properties of galaxies in order to keep the model parameters within realistic ranges. These priors are a function of redshift, which effectively let the templates evolve with redshift. It also applies template error functions to reduce systematic biases in the model templates and also to assign uncertainties to the templates. The code is run using the *grizy* CModel photometry. The redshift and physical parameters are estimated by marginalizing over all the other parameters. The quoted uncertainties in the physical properties thus include uncertainties in photometric redshifts. Details of the calibration of the codes and the data products are described in the photo-z release paper (Tanaka et al. in prep.). It is also noted that there is a known bias in stellar mass in Mizuki which is about a factor of 2 larger than the mass in COSMOS at $z \sim 1$ (Tanaka 2015).

2.4 K-correction, Completeness Limit of Stellar Mass, and Star Formation Rate

Our approach to computing the K-correction follows a similar method described in Willmer et al. (2006) to relate the observed color and magnitude at redshift z to the rest-frame color and magnitude based on empirical templates from Kinney et al. (1996). The detail description can be found in Willmer et al. (2006) as well as in Lin et al. (2014). In short, for a given redshift, we perform a polynomial fit between the K-correction term and a pair of adjacent observed color base on Kinney et al. templates, where the K-correction term is chosen to be the observed bandpass closest to the desired rest-frame quantity. Different input redshifts lead to different fitting results or polynomial formulas, and a table of fitting polynomial values can then be constructed and be applied to galaxies depending on their redshift in the range of $0 < z < 1.45$.

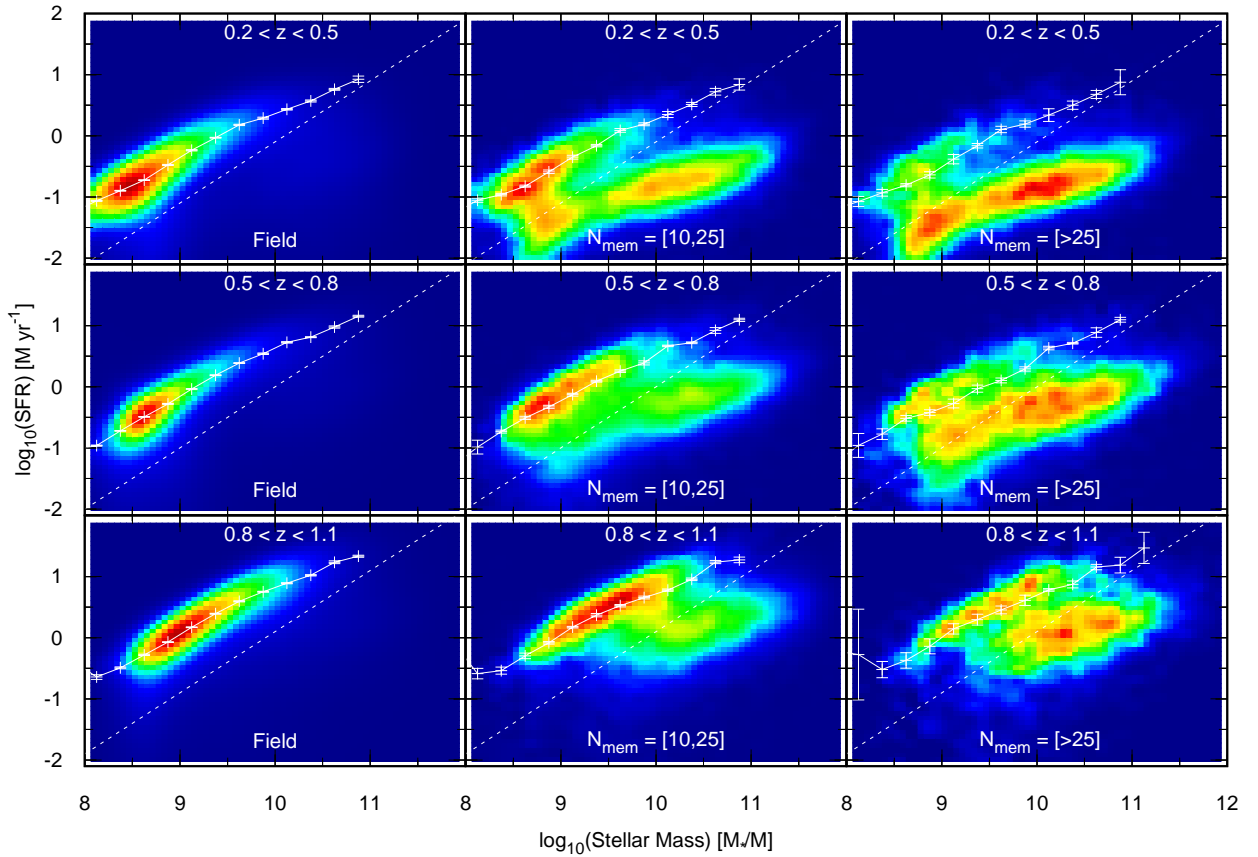


Fig. 1. The images show the color-coded number densities of stacked galaxies for the SFR- M_* relation in three redshift ranges from [0.2,0.5], [0.5, 0.8] to [0.8, 1.1] (from the top to the bottom) and in three different environments, including the field (left), groups (middle), and clusters (right), respectively. The color scale in the color-bar is proportional to the number counts in each cell normalized by the cell with the maximum count. The diagonal lines represent the boundaries to separating star-forming and quiescent populations. They are $sSFR = 10.1$ in $0.2 < z < 0.5$, 10 in $0.5 < z < 0.8$, and 9.9 in $0.8 < z < 1.1$, respectively. The white solid lines with error-bars, estimated using the jack-knife resampling from eight sub-samples, denote the median values of SFRs at different stellar masses. We can qualitatively learn the redshift evolution of galaxies in three distinct environments, and at the same redshift, the differences of galaxy distributions in the SFR- M_* space in different environments to see the environmental impact.

The estimation of the stellar mass limit follows the method described in Lin et al. (2014). We first compute the rest-frame quantities for galaxies at a given redshift based on their 5 limiting magnitudes in the observed HSC bands utilizing the K-correction method illustrated previously. Adopting the empirical formula obtained by Lin et al. (2007), we then convert the rest-frame magnitudes and colors to the corresponding stellar mass. It is known that at a fixed rest-frame magnitudes, the redder color a galaxy, the higher mass. By taking the reddest colors of star-forming and quiescent populations, we derive their corresponding mass limits. In this way, we find that the mass limits $\log_{10}(M_*/M_\odot)$ are 8.6 (8.2), 9.3 (8.9), 9.7 (9.3) and 10.3 (9.8) for red (blue) galaxies at $z \sim 0.2, 0.5, 0.8$, and 1.1, respectively.

We compute the SFR following the approach described in Mostek et al. (2012). The SFR is parameterized as functions of rest-frame optical B magnitudes M_B and (U-B) color and calibrated against SED-fit SFR from UV/optical bands in the

All-Wavelength Extended Groth Strip International Survey for both red sequence and blue cloud galaxies in the $0.7 < z < 1.4$ redshift range. The calculated SFRs are found to agree well with an $L[O_{II}]-M_B$ SFR calibration commonly used in the literature by considering a correction for the measured values M_B from DEEP2 galaxies to include a dimming factor of $Q = 1.3$ magnitudes per unit redshift (Mostek et al. 2012). In this work, we adopt the fitting formula using the rest-frame optical M_B , (U-B), and a second order (U-B) color as fit parameters and the fit coefficients can be found in Table 3 in Mostek et al. (2012). It is reported in Mostek et al. (2012) that the SFR uncertainties depend on colors of galaxies. Although the method gives more precise SFRs for star-forming galaxies and less accurate SFRs for quiescent ones, it uncovers the SFR of galaxies with a wide range of star formation activities. In this study, the main emphases are the comparisons of star formation rate for star-forming galaxies and the quiescent fraction in different environ-

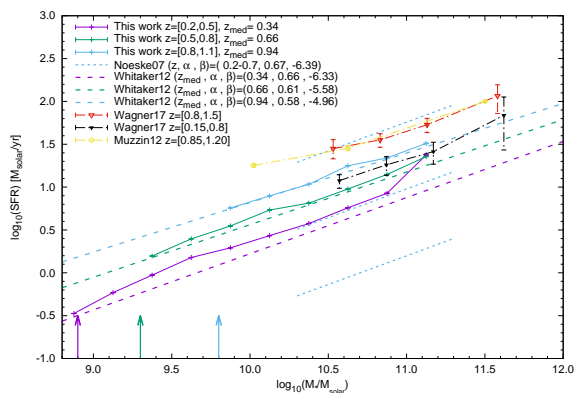


Fig. 2. The median SFR of the SF main sequence in the field in redshift range of $0.2 < z < 0.5$ (purple), $0.5 < z < 0.8$ (green), and $0.8 < z < 1.1$ (blue) from this work (solid lines) and from Whitaker et al. (2012) (dashed lines), respectively. The results of the SF main sequence in the field from Wagner et al. (2017) (red and black triangles), Muzzin et al. (2012) (yellow), and Noeske et al. (2007) with upper and lower limits (blue dotted lines) are also included for comparisons. The purple, green, and blue arrows denote the mass completeness limit for SF galaxies at $z = 0.5$, 0.8 , and 1.1 . Our results, in general, are in agreement with the results from literature.

ments. The larger uncertainty in the SFR estimate for quiescent objects has little impact on our results.

The sSFR, defined as SFR/M_* , is used to separate star-forming and quiescent populations. In this work, the separating thresholds we apply are $\log_{10}(\text{sSFR}) = -10.1 \text{ yr}^{-1}$ in $0.2 < z < 0.5$, -10.0 yr^{-1} in $0.5 < z < 0.8$, and -9.9 yr^{-1} in $0.8 < z < 1.1$.

2.5 Method

By construction, the CAMIRA cluster catalog only contains red cluster members. In order to probe the properties of general populations in clusters, we perform the stacking analysis and correct for the background/foreground contaminations. The details of the method are discussed and illustrated in Jian et al. (2017). In short, the contaminated galaxy properties around the cluster centers during stacking can be statistically removed by subtracting the same galaxy properties of a mean local background, selected either from random positions or from annuli between r_1 and r_2 , where r_1 and r_2 are the inner and the outer comoving radii around cluster centers, respectively. For each cluster, we project galaxies around its center onto a plane within a redshift width equal to the photo- z accuracy of the galaxy sample, i.e. $|z - z_{\text{grp}}| \leq \sigma_{\Delta z}/(1+z_s)$, where z , z_{grp} , and $\sigma_{\Delta z}/(1+z_s)$ are galaxy, group redshift, and photo- z accuracy, respectively. For galaxies on this projected plane, their redshift is adjusted to the cluster redshift for k-correction. Galaxies within a projection radius r_p 1.5 Mpc from the center are considered as the contaminated cluster galaxy sample. The corrected sample can be obtained by subtracting the contaminated cluster galaxy sample with an area-normalized background sample. In this

work, we select comoving r_1 and r_2 to be 8.0 and 10.0 Mpc, respectively.

3 Results

3.1 Main Sequence Properties

The main sequence indicates the tight correlation between galaxy SFR and M_* for star-forming (SF) galaxies. In Figure 1, we show the color-coded number density plots of stacked galaxies for the SFR- M_* relation in 3 redshift bins, $[0.2, 0.5]$, $[0.5, 0.8]$ and $[0.8, 1.1]$ (from the top to the bottom), and in the environment of the field (left), groups (middle), and clusters (right). The diagonal dashed lines separate the star-forming or the main sequence (above) and quiescent galaxies (below) with $\log_{10}(\text{sSFR}) = -10.1 \text{ yr}^{-1}$ in $0.2 < z < 0.5$, -10.0 yr^{-1} in $0.5 < z < 0.8$, and -9.9 yr^{-1} in $0.8 < z < 1.1$. The colors are scaled with the number counts in each cell normalized by the cell with the maximum count. The solid white lines with error-bars give the median SFRs of SF galaxies in different redshifts and environments as a function of the stellar mass. The error-bars are estimated from eight sub-samples using the jackknife resampling method. It is seen that the distributions of field galaxies have a distinct appearance from those of group or cluster galaxies. In the field, the presence of star-forming galaxies is so prominent that quiescent galaxies can almost be neglected for all masses. By contrast, in groups or clusters, quiescent galaxies become the dominant ones for mass roughly larger than $10^{9.5-10} M_{\odot}$. In general, our results are in good agreement with the conclusions from previous studies that the group or cluster environment has a higher red fraction of galaxies than the field environment (Gerke et al. 2007; Giodini et al. 2012). In addition, the evolution of field, group, and cluster galaxies can also be seen clearly. Qualitatively, the main sequence of SF field galaxies has lower sSFR as it evolves from high redshift to low redshift. The fraction of the quiescent population in groups and clusters becomes higher with the decreasing redshift, and at the same redshift, the quiescent population in clusters is more prominent than in groups, evident the hosting environmental effect.

To further quantitatively understand our results, the main sequence at different redshift is compared with that from Whitaker et al. (2012) in Figure 2. The purple, green, and blue solid lines represent the median SFR in three redshift ranges from low to high redshift in our sample, respectively. The three dashed lines plot the fitting lines at median redshifts in our three bins, $z_{\text{med}} = 0.33$, 0.68 , and 0.93 , using the best-fit parameters from Whitaker et al. (2012). We adopt the mass conversion factors from Speagle et al. (2014) for stellar mass assuming different initial mass function (IMF), i.e., $M_{*,K} = 1.06 M_{*,C} = 0.62 M_{*,S}$, where S, C, and K, are referred to Salpeter, Chabrier, and Kroupa IMFs. The dotted blue line gives the best-fit results

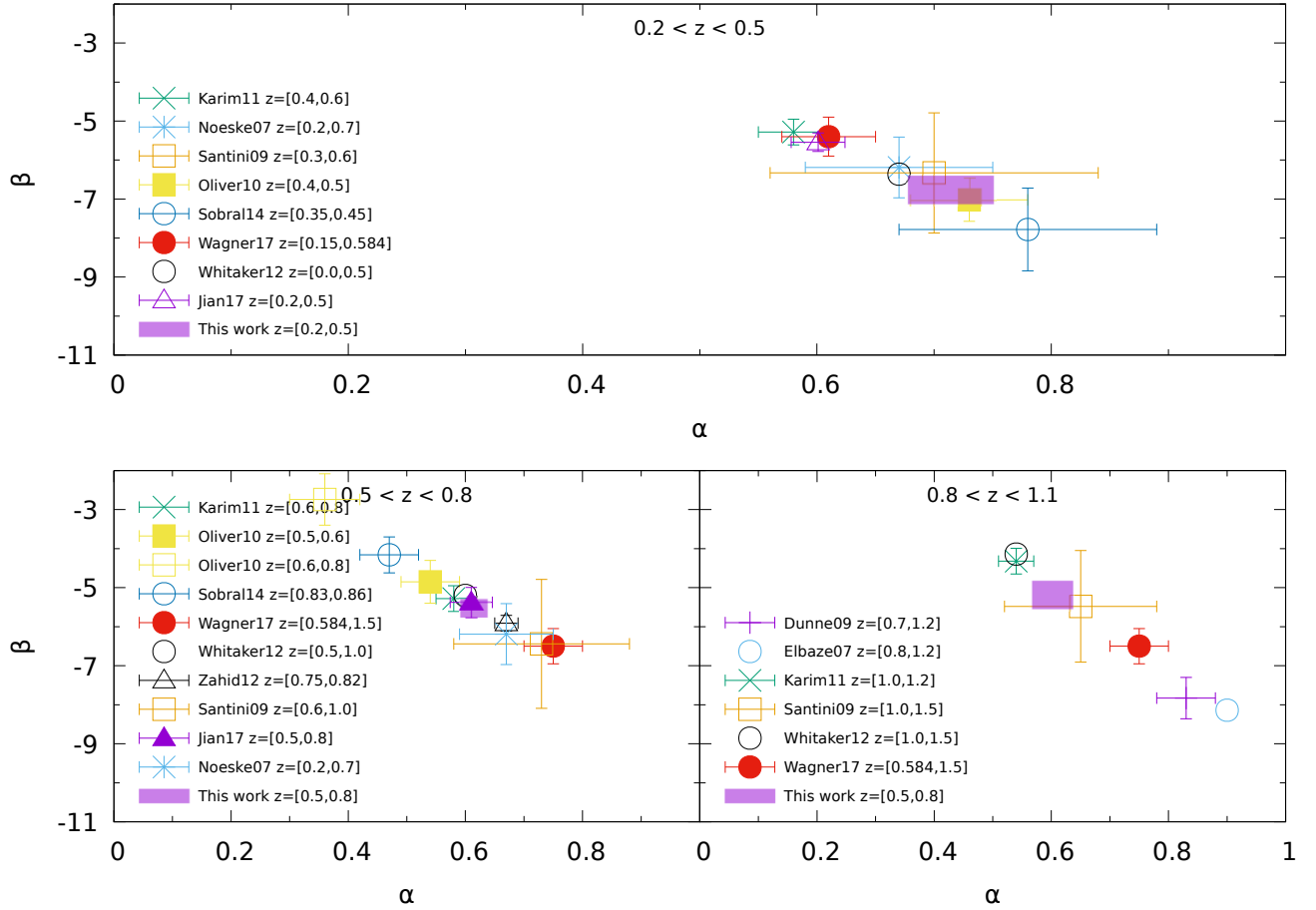


Fig. 3. Best-fit parameters α and β in Equation 1 for SF galaxies are plotted in three redshift ranges. This figure is based on the work by Speagle et al. (2014), who compile and calibrate the best-fit parameters from literatures including Elbaz et al. (2007), Noeske et al. (2007), Dunne et al. (2009), Santini et al. (2009), Oliver et al. (2010), Karim et al. (2011), Whitaker et al. (2012), Zahid et al. (2012), and Sobral et al. (2014). Additionally, we add the results from Wagner et al. (2017), Jian et al. (2017) and this work. The best-fit parameters from Whitaker et al. (2012) are without uncertainties and shown by open circles.

from Noeske et al. (2007) in $0.2 < z < 0.7$. The yellow diamonds with error-bars are the SFRs of SF cluster galaxies in redshift range between 0.15 and 0.8 from Muzzin et al. (2012), and the black and red triangles represent the SFRs of SF cluster galaxies in $0.15 < z < 0.8$ and $0.8 < z < 1.5$, respectively. It is seen that the best-fit slopes and magnitudes of the SF main sequence in our sample in three redshift ranges agree well with those in Whitaker et al. (2012) and Noeske et al. (2007), and are in broad agreement with those from Wagner et al. (2017). Additionally, we quantify the main sequence by fitting the data with a formula of a power law, i.e.

$$\log_{10}(\text{SFR}/M_{\odot}\text{yr}^{-1}) = \alpha \log_{10}(M_{*}/M_{\odot}) + \beta, \quad (1)$$

where α and β are the slope and normalization, respectively. In Figure 3, our best-fit α and β for SF field galaxies in three different redshift ranges are plotted with a selection of literature best-fit parameters from a sample of 25 studies in the redshift range of $0 < z < 6$, compiled and calibrated by Speagle et

al. (2014), including Elbaz et al. (2007), Noeske et al. (2007), Dunne et al. (2009), Santini et al. (2009), Oliver et al. (2010), Karim et al. (2011), Whitaker et al. (2012), Zahid et al. (2012), and Sobral et al. (2014). All the above published best-fit parameters are standardized to a Kroupa IMF in Speagle et al. (2014). Besides, we add the results from Wagner et al. (2017) for SF cluster galaxies, and from Jian et al. (2017) for SF field galaxies. Our best-fit parameters are in good agreement with those from other published works, indicating the robustness of our results.

3.2 Redshift Dependence

3.2.1 sSFR of SF galaxies, $\text{sSFR}_{\text{SF}}(z)$

There have been many previous studies to discuss and compare the evolution of the main sequence in different environments (Koyama et al. 2013; Lin et al. 2014; Erfanianfar et al. 2016; Wagner et al. 2017; Jian et al. 2017). Taking the advan-

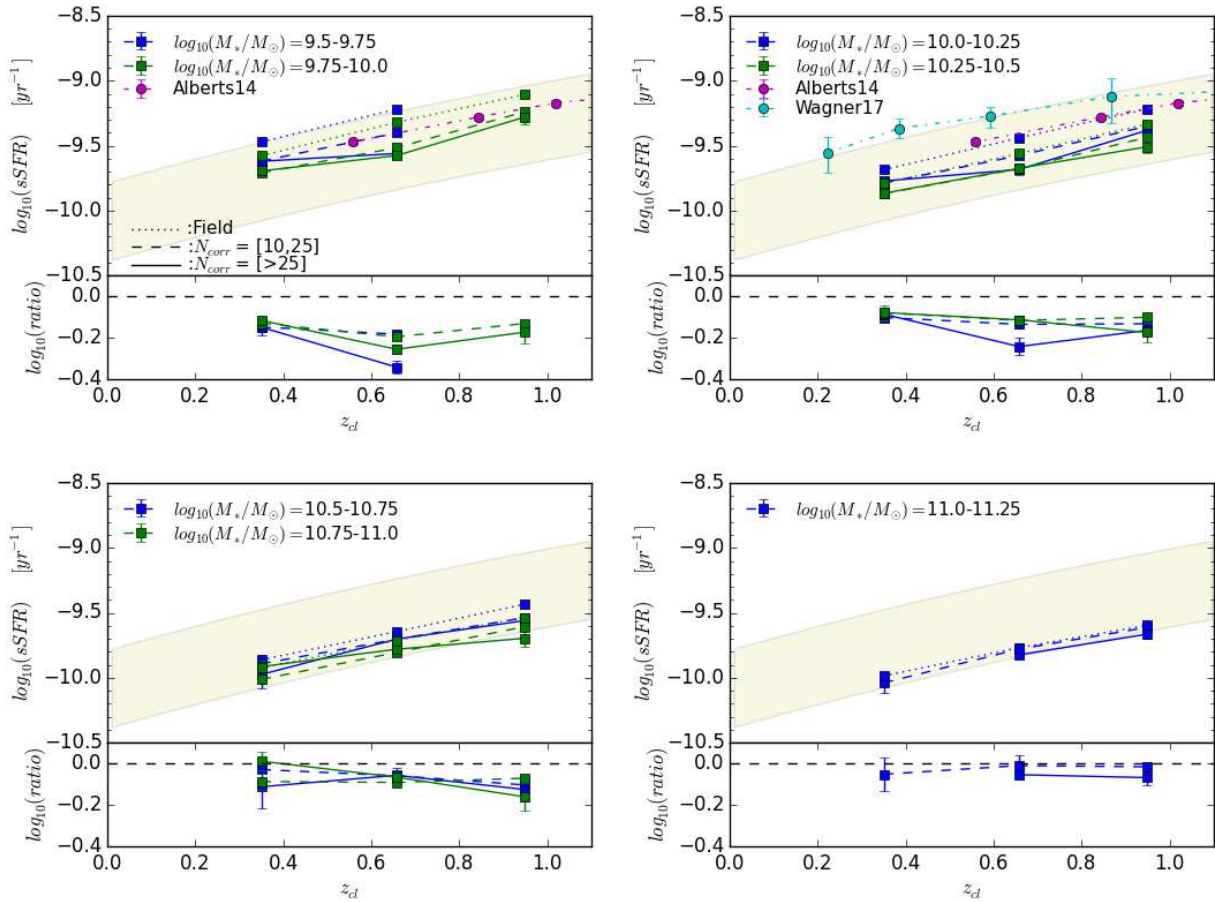


Fig. 4. Top: The median sSFR of SF galaxies as a function of redshift in the field (dotted), groups (dashed), clusters (solid), respectively. Bottom: The logarithmic ratio of sSFR for group to field galaxies (dashed), and for cluster to field galaxies (solid). In addition, the red and cyan circles denote the sSFR of SF galaxies in the field from Alberts et al. (2014) for $M_* > 1.3 \times 10^{10} M_\odot$ and in clusters from Wagner et al. (2017) for $M_* > 10^{10.1} M_\odot$, respectively. The yellow shade region gives the boundaries of the infrared Main Sequence as defined in Elbaz et al. (2011). In the upper left panel, the data points in the redshift range of $0.8 < z < 1.1$ for the mass bin 9.5-9.75 are removed due to the mass incompleteness. The trend that the sSFR decreases with the decreasing redshift and the decreasing level for the same redshift range in our results are in good agreement with other works although a systematics is seen.

tage of the large and deep HSC sample, we are able to explore the same subject with better statistics and low mass galaxies. In Figure 4, the median sSFRs of the star-forming galaxies in field (dotted lines), group (dashed lines), and cluster (solid line) environments on the top, and the sSFR ratio of group to field galaxies (dashed lines) and that of cluster to field galaxies (solid lines) on the bottom are plotted as a function of redshift in different mass ranges separated in four panels. The yellow shaded region denotes the infrared main sequence as defined in Elbaz et al. (2011), and is in the range of $13(13.8 \text{ Gyr} - t)^{-2.2} < \text{sSFR} < 52(13.8 \text{ Gyr} - t)^{-2.2}$, where t is the look-back time. The red data circles mark the sSFR of the star-forming galaxies in the field from Alberts et al. (2014) with stellar mass limit $M > 1.3 \times 10^{10} M_\odot$. Four cyan circles with error-bars are from Wagner et al. (2017) for SF cluster galaxies with mass larger

than $\log_{10}(M_*/M_\odot) = 10.1$. From Figure 4, our results show good consistency with that in Elbaz et al. (2011) and slightly shallower at low z than that in Alberts et al. (2014). It is seen that the decrease of the sSFR of the SF main sequence for field galaxies is ~ 0.45 dex from $z = 1.1$ to 0.2 for all mass bins, possibly due to a global decline in the gas contents. At fixed masses, the decrease level is very similar to cluster and group galaxies between the same redshift range but a systematics is seen < 0.4 dex for clusters and < 0.2 dex for groups. That is, the decrease of sSFRs for the group to field galaxies and for the cluster to field ones is independent of redshift. However, the decrease appears to depend on stellar mass, being larger for less massive galaxies. Our results are in agreement with those in Koyama et al. (2013) that the difference in the SFR- M_* relation between cluster and field SF galaxies is ~ 0.2 dex since $z \sim 2$.

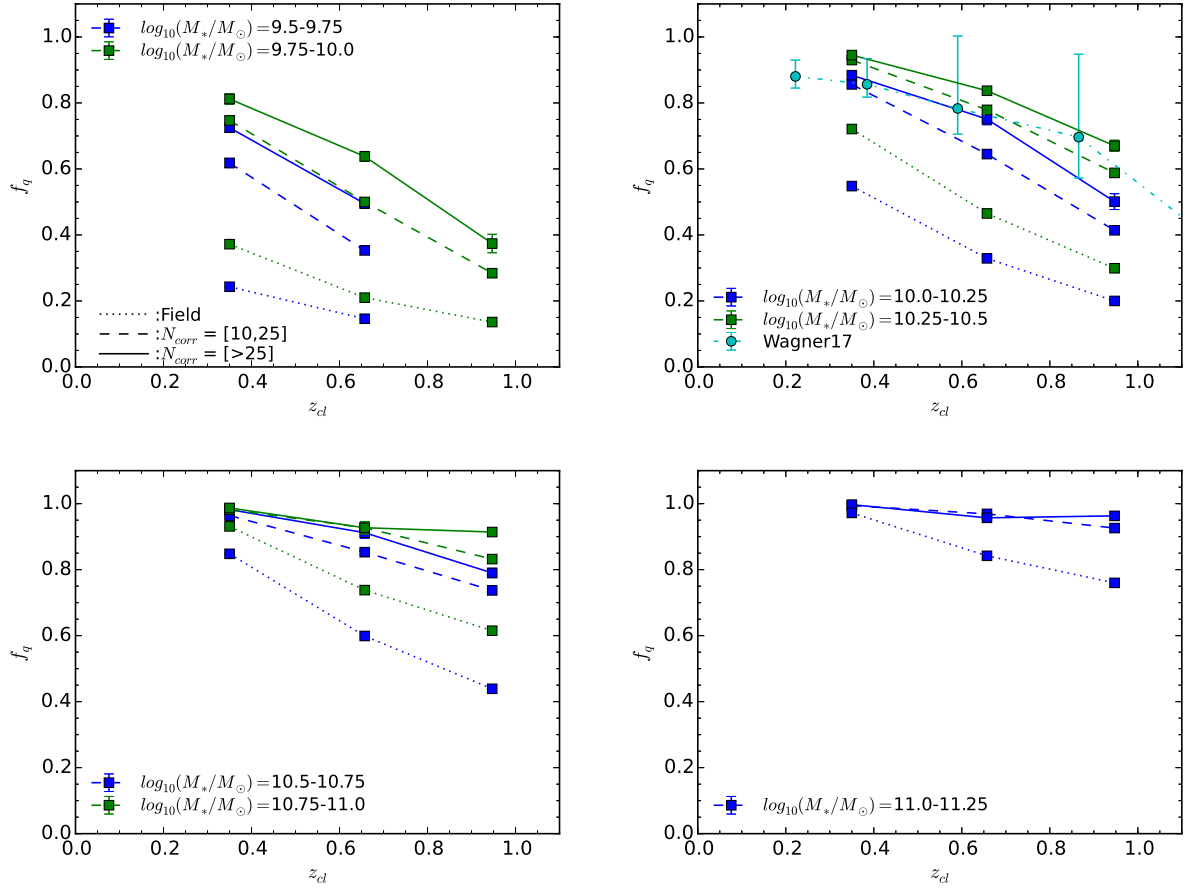


Fig. 5. The redshift evolution of the quiescent fractions (f_q s) for field (dotted), group (dashed), cluster (solid) galaxies, respectively. Similar to the upper left panel in Figure 4, the data points in the high redshift bin for the mass bin 9.25-9.5 are removed due to the mass incompleteness. The Butcher-Oemler effect (Butcher & Oemler 1984) is clearly seen but with a mass dependence. The effect is stronger for less massive galaxies and less for massive galaxies. For comparisons, we also add the f_q results from Wagner et al. (2017) (cyan circles) with $M_* > 10^{10.1} M_\odot$ in the upper right panel. It is seen that our result is in agreement with that from Wagner et al. (2017).

3.2.2 Quiescent Fraction, $f_q(z)$

Under the stellar mass control, the redshift dependence of the quiescent fractions (f_q) for field (dotted lines), group (dashed lines), and cluster (solid lines) galaxies is explored in Figure 5. For comparison, the results from Wagner et al. (2017) (cyan circles) with $M_* > 10^{10.1} M_\odot$ are also plotted in Figure 5. Globally, the f_q increases with decreasing redshift, consistent with the Butcher-Oemler effect (Butcher & Oemler 1984). However, depending on the galaxy masses, their effect can be significantly different. For high-mass galaxies, the Butcher-Oemler effect is weak and nearly negligible. On the other hand, the effect is stronger for low-mass ones, consistent with results in Li et al. (2012). For low-mass galaxies, the increase of f_q is about 3 times larger from high $z \sim 0.95$ to low $z \sim 0.35$. In addition, the cluster downsizing effect that clusters with larger halo mass show greater quiescent fraction is also evident

in our sample. Our redshift evolution trend is similar to that in Wagner et al. (2017), and the f_q derived for our sample in $\log_{10}(M_*/M_{\text{odot}}) = 10.2-10.5$ (the blue solid line in upper right panel) appears to also be consistent with those in Wagner et al. (2017).

3.2.3 Quenching Efficiency, $\varepsilon(z)$

We also compute the environmental quenching efficiency, $\varepsilon^{\text{envi}} = (f_q^{\text{cluster}} - f_q^{\text{field}})/(1 - f_q^{\text{field}})$, similar to the definition in (Peng et al. 2010), as a function of redshift in different mass bins to quantify the excess of quenching due to pure environmental effects in Figure 6. In general, the quenching efficiency increases with the decreasing redshift, and also increases with the increasing mass at fixed redshift. However, the slope of the quenching efficiency decreases with the increasing masses, implying that the quenching effect is stronger for less mas-

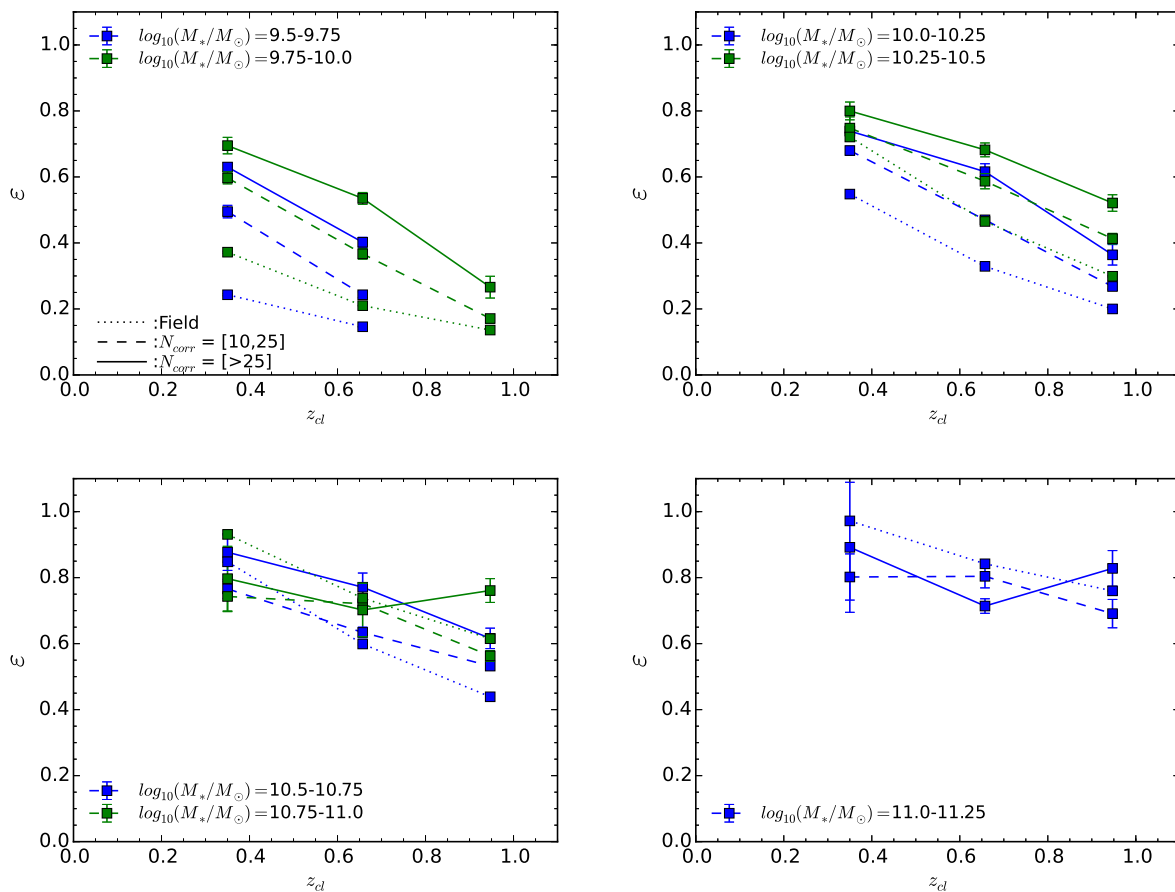


Fig. 6. Similar to Figure 4 and 5, the quenching efficiency ε is plotted as a function of redshift for different mass ranges in four panels for field (dotted), group (dashed), and cluster (solid) galaxies, respectively. In general, the slope of the quenching efficiency decreases with the increasing masses, implying that the quenching effect is stronger for less massive galaxies.

sive galaxies. The redshift dependence becomes weaker for the high-mass galaxies, likely due to being red and dead already for most of the massive galaxies at high redshifts. In addition, it is seen that the environmental quenching in clusters is larger than that in groups, indicating that the hosting environment has a significant effect on the star formation quenching.

3.3 Stellar Mass Dependence

3.3.1 sSRF of SF galaxies, $s\text{SFR}_{\text{SF}}(M_*)$

In Figure 7, the sSFRs of SF galaxies are plotted as a function of the stellar mass M_* in different hosting environments and redshift ranges. In the upper left panel, the median sSFR of SF field galaxies is shown in redshift range of $0.2 < z < 0.5$ (dashed line), $0.5 < z < 0.8$ (solid one), and $0.8 < z < 1.1$ (dotted line) for comparisons, respectively. For the other three panels on top-right, bottom-left, and bottom-right, the sSFRs

of SF field (black pluses), group (blue squares), cluster (green circles) galaxies are plotted on the top while the logarithmic ratio of sSFR for SF group to field galaxies (blue squares) and that for SF cluster to field ones (green circles) are displayed on the bottom. Additionally, the red pluses, squares, and circles denote the sSFR of SF field, group, and cluster galaxies in $0.5 < z < 0.8$ from Lin et al. (2014), respectively. The cyan circles are the sSFRs of SF cluster galaxies in $0.15 < z < 0.8$ and in $0.8 < z < 1.5$ from Wagner et al. (2017), and the purple pluses and circles are those of SF field and cluster galaxies in $0.85 < z < 1.2$ from Muzzin et al. (2012).

In general, the median sSFR of group or cluster galaxies decreases from that of field ones, implying a slow quenching effect acting in dense environments. We found that there is a weak dependence on the stellar mass of the sSFR deficit relative to the field, which is < 0.2 dex in groups and < 0.4 dex in clusters. The larger deficit seen in cluster galaxies as opposed to group

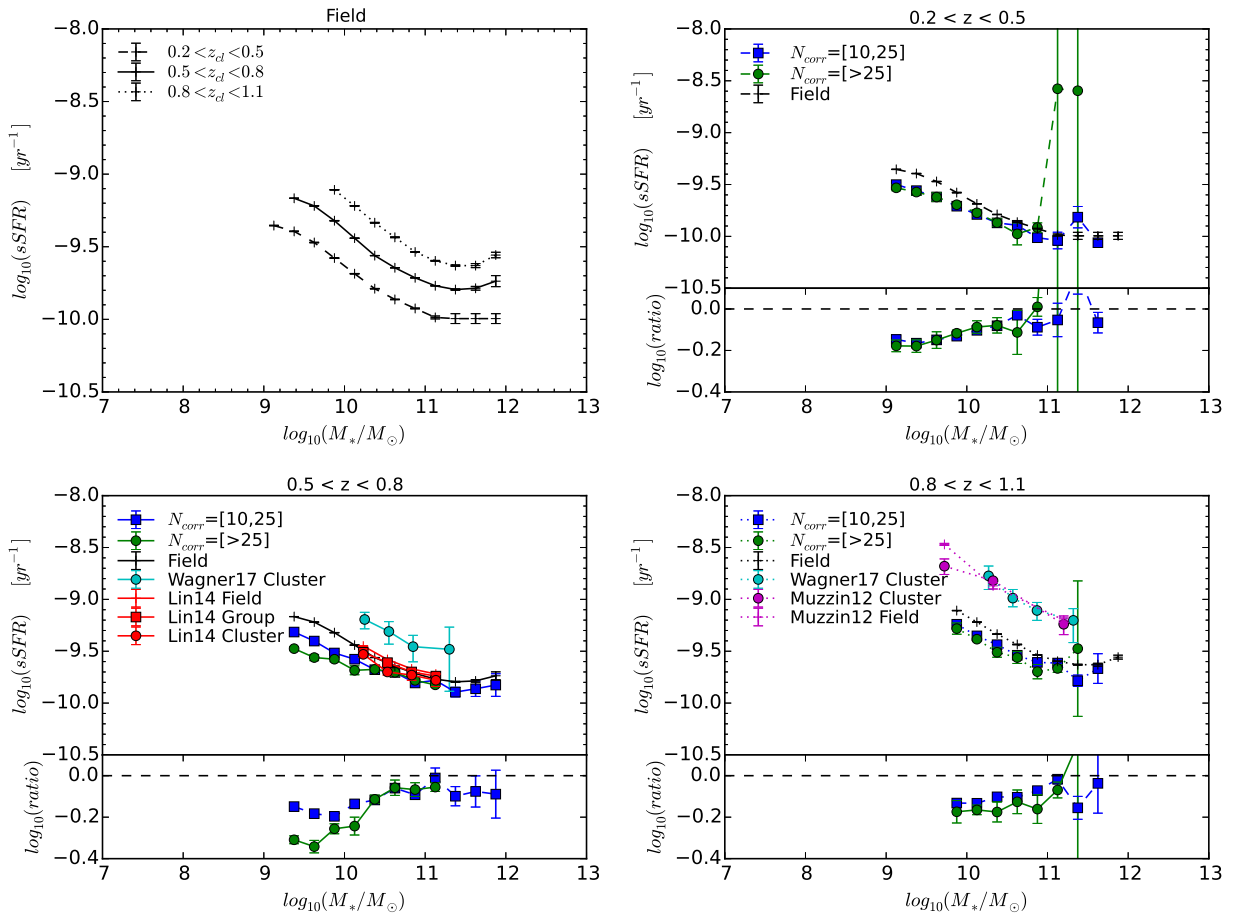


Fig. 7. Similar to Figure 4, but the sSFRs of SF galaxies are shown as a function of stellar mass. In the upper left panel, the sSFR of SF field galaxies in redshift range of $0.2 < z < 0.5$, $0.5 < z < 0.8$, and $0.8 < z < 1.1$ is represented by the dashed, solid, and dotted line, respectively. The other three panels plot the sSFRs of SF field (black pluses), group (blue squares), and cluster (green circles) galaxies on the top, and the logarithmic ratio of sSFR for group to field galaxies (blue squares), and for cluster to field galaxies (green circles) on the bottom. For comparisons, we also include the sSFR results from Lin et al. (2014) in the redshift range of $0.5 < z < 0.8$ for SF field (red pluses), group (red squares), and cluster (red circles) galaxies. In addition, the sSFR results are added as well from Muzzin et al. (2012) for SF field (purple pluses) and cluster (purple circles) galaxies in redshift range of $0.85 < z < 1.2$, and from Wagner et al. (2017) for SF cluster galaxies (cyan circles) in redshift range of $0.15 < z < 0.8$ (bottom left) and $0.8 < z < 1.5$ (bottom right).

galaxies suggests a stronger environmental quenching effect in clusters than in groups. It is worth noting that the decreases are slightly larger from what was found in Lin et al. (2014), who found no significant sSFR reduction of SF galaxies in the groups and $\sim 17\%$ (0.23 dex) sSFR decrease for the SF galaxies in the clusters relative to the field galaxies. However, we note that the halo mass binning is $10^{13.6-14.2} M_{\odot}$ for groups and $10^{>14.2} M_{\odot}$ for clusters in this work while it is $10^{13.4-14.0} M_{\odot}$ for groups and $10^{>14.0} M_{\odot}$ for clusters in Lin et al. (2014). The larger sSFR offset seen in this work may be attributed to the greater masses of the groups and clusters probed in our analysis, since larger sSFR reduction is expected in more massive clusters. In addition, less massive groups normally suffer from the more serious foreground and background contaminations

and the real group signals can be easily smeared out, leading to the less sSFR reduction. In the high redshift (bottom-right) panel, although there seems to have a systematic between our results and the results from Muzzin et al. (2012) and Wagner et al. (2017) for the absolute sSFR values, the decreasing trend of the sSFR with the increasing mass in our sample agrees well with them. Besides, it is noticed that our results for the sSFR reductions are in broad agreement with those from Muzzin et al. (2012).

3.3.2 Quiescent Fraction, $f_q(M_*)$

The quiescent fraction (f_q) is investigated as a function of M_* in Figure 8. Similar to Figure 7, the upper-left panel shows the f_q for field galaxies in three redshift ranges, and the other three

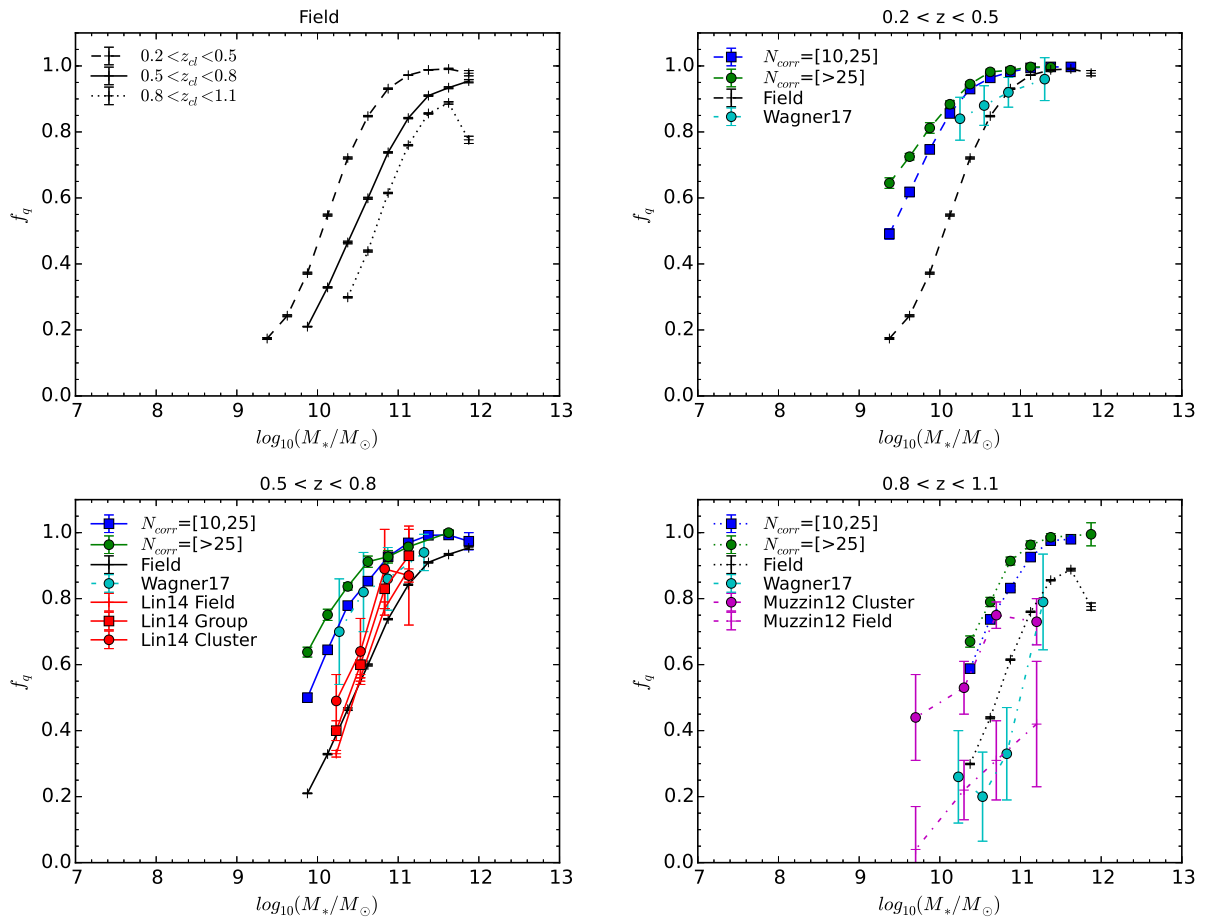


Fig. 8. The quiescent fraction f_q s as a function of stellar mass. In upper left panel, the f_q s are plotted for field galaxies in three redshift bins while the other three panels show the f_q s of field (black pluses), group (blue squares), and cluster (green circles) galaxies in redshift range of $0.2 < z < 0.5$ (upper right), $0.5 < z < 0.8$ (bottom left), and $0.8 < z < 1.1$ (bottom right). The red pluses, squares, and circles denote the f_q s for field, group, and cluster galaxies, respectively, from Lin et al. (2014) in redshift range of $0.5 < z < 0.8$. The cyan circles are data points from Wagner et al. (2017) for cluster galaxies in redshift range of $0.15 < z < 0.41$ (upper right), $0.41 < z < 0.8$ (bottom left) and $0.8 < z < 1.5$ (bottom right). The purple pluses and circles represent the f_q s for field and cluster galaxies, respectively, from Muzzin et al. (2012) in redshift range of $0.85 < z < 1.2$.

panels give the comparisons of f_q for the field, group, and cluster galaxies in one redshift range per one panel. Results of f_q are included for comparisons from Muzzin et al. (2012) for field and cluster galaxies in redshift range of $0.85 < z < 1.2$, from Lin et al. (2014) for field, group, and cluster galaxies in $0.5 < z < 0.8$, and from Wagner et al. (2017) for cluster galaxies in $0.15 < z < 0.41$, $0.41 < z < 0.8$, and $0.8 < z < 1.5$. It is seen that the quiescent fraction depends strongly on mass and less strongly on redshift and the hosting environment. At high redshifts, the f_q difference at fixed mass between group and cluster galaxies is small and gradually becomes larger with the decreasing redshift, indicating that the environmental quenching effect has a redshift dependence. In addition, the typical downsizing effect in which less massive galaxies are more star-forming continues down to $\sim 10^9 M_\odot$. Moreover, at low mass, it is found that the

red sequence is still visible in groups or clusters with respect to the field, implying that the environmental quenching can still effectively stop star-formation for low mass galaxies. It is noticed that the f_q in this work is higher compared to those from Lin et al. (2014) and Wagner et al. (2017). Besides the greater cluster masses used in this work (see the discussion in the previous section 3.3.1), it is also likely that the CAMIRA cluster finding is based on the red sequence method and preferentially select clusters with high f_q . In the high redshift range, our f_q s broadly agree with those from Muzzin et al. (2012). However, lower f_q s are found in Wagner et al. (2017), likely due to the fact that their sample includes galaxies up to $z \sim 1.5$.

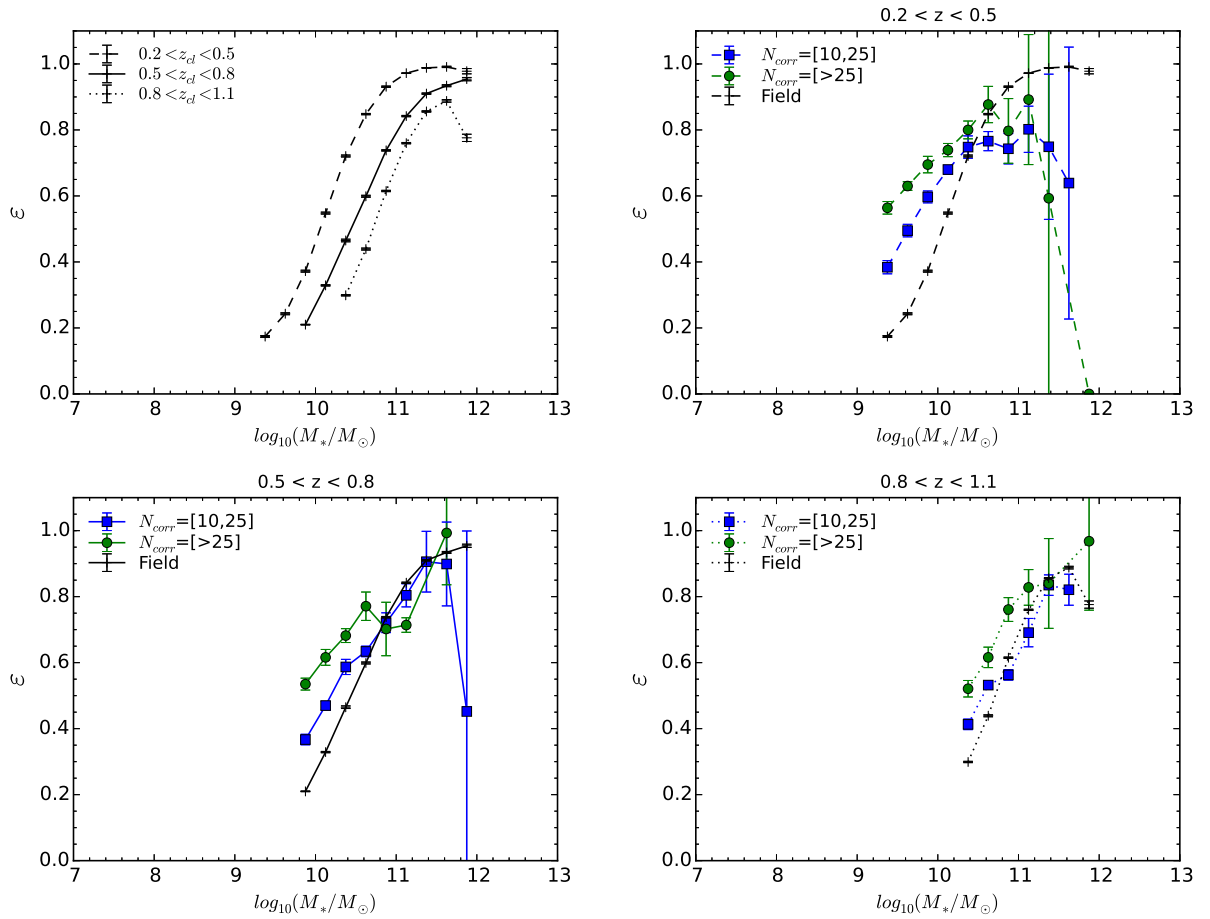


Fig. 9. The quenching efficiency ε_s as a function of stellar mass. Similar to Figure 7 and 8, the ε_s of field galaxies in three redshift bins are shown in the upper left panel while the other three panels plot the ε_s of field (black pluses), group (blue squares), and cluster galaxies (green circles) in three redshift ranges, respectively. It is clearly seen that the transition masses from the dominance of the environment quenching to that of the mass quenching are $\log_{10}(M_*/M_\odot) \sim 10.4$ in groups and ~ 10.6 in clusters.

3.3.3 Quenching Efficiency, $\varepsilon(M_*)$

The environmental quenching efficiency is schemed as a function of stellar mass in Figure 9 in order to better quantify the excess of quenching due to pure environmental effects. The panel arrangement is similar to that in Figure 7 and 8. In the upper-left panel, the quenching efficiency from field galaxies, or the mass quenching efficiency assuming that field galaxies are purely quenched by their masses, are displayed in three redshift ranges. The other three panels present the comparisons among the field, group, and cluster galaxies per redshift bin. It is clearly seen that both the mass and environmental quenching increases with increasing stellar mass. However, high mass galaxies are dominated by the mass quenching while low mass galaxies are quenched primarily due to the environmental quenching. The transition mass where the dominance of the mass and environmental quenching switches is recognized at $\log_{10}(M_*/M_\odot) \sim$

10.4 in groups and 10.6 in clusters in the lowest redshift range of $0.2 < z < 0.5$, in good agreement with the results from Lin et al. (2014). This implies that the environmental quenching in clusters is more prominent than that in groups since it can quench more massive galaxies than in groups.

4 Conclusion and Discussion

In this work, we probe galaxies down to $i \sim 26$, two magnitudes deeper than that in our previous works (Lin et al. 2014; Jian et al. 2017), and extend our results to redshift 1.1, enabling us to study the cosmic evolution of the star formation activity. Due to the exceptional deep depth of our sample, the stellar mass completeness limit can be pushed to $\log_{10}(M_*/M_\odot) = 9.8$ and 10.3 at $z \sim 1.1$ for star-forming and quiescent galaxies, respectively. That is, we are able to explore the quenching status of

lower-mass star-forming galaxies which have not explored in our previous works. Additionally, the HSC Wide 16A data are collected from a survey area ~ 174 square degree to offer good statistics even for galaxies at the high-mass end. In other words, we can constrain the results on high mass galaxies more robustly as opposed to previous studies. The main results can be summarized below:

1. The sSFR of star-forming galaxies decreases with cosmic time, regardless the environments. The sSFR is lower in groups and clusters than in the field by ~ 0.1 dex and ~ 0.2 – 0.3 dex, respectively. The drop of sSFR in group/cluster environments is insensitive to the redshift and is more significant for low mass galaxies.

2. The quiescent fraction is a strong function of stellar mass in all environments, being greater for higher mass galaxies. The Butcher-Oemler effects are seen in all environments and are more prominent for low mass galaxies.

3. Both the environment and stellar mass quenching efficiencies increase with the stellar mass. However, the environment quenching dominates over the stellar mass quenching for low mass galaxies.

At a fixed stellar mass, we find that the decrease in the sSFR of star-forming group or cluster galaxies to field ones is 0.1–0.3 dex and is more prominent in cluster environments. This implies that galaxies in clusters likely experience a long timescale (or slow) quenching effect that gradually reduces the SFR of star-forming galaxies. Although the gas contents and hence the star formation rate of galaxies vary with redshifts, we find that the offsets in the sSFR in groups/clusters, as opposed to the field, are comparable at different redshifts, in agreement with the results found by Koyama et al. (2013). This implies that the slow quenching mechanism acting on groups/clusters is likely universal in the redshift range of $0.2 < z < 1.1$.

In addition, it is found in this work that the transition masses from environment quenching to the mass quenching are $10^{10.4} M_{\odot}$ and $10^{10.6} M_{\odot}$ in groups and clusters, respectively, in the lowest redshift bin of $0.2 < z < 0.5$, in good agreement with the results from Lin et al. (2014). The greater transition mass in clusters suggests that the environment effects are more important in clusters than in groups and have an effect even for massive galaxies. It is also noticed that the red fraction for the most massive galaxies is comparable between the field and group/cluster environments. This suggests that the star formation of those massive galaxies beyond the transition mass are likely already stopped and being red and dead before they enter the cluster-like environments. Conversely, the environmental quenching dominates the mass quenching in low mass galaxies below the transition mass in groups or clusters down to the mass completeness limit of $10^{8.6} M_{\odot}$ at $z \sim 0.2$, and the environmental quenching effect in clusters is stronger than that in groups. At this low mass regime, the red sequence is still visi-

ble in groups or clusters with respect to the field, suggesting that the environmental quenching can still effectively stop star-formation for low mass galaxies.

Koyama et al. (2017) recently present their results discussing the environmental dependence of color, stellar mass, and sSFR of H_{α} -selected galaxies in twin clusters in the DEEP2-3 field at $z = 0.4$. One important finding in their work is that H-selected galaxies reveal color-density or color-radius correlations, but their stellar masses or sSFRs are independent of environments. The conclusion appears to be inconsistent with our result that there is a systematical reduction of sSFR for SF galaxies in groups or clusters by 0.1 – 0.3 dex with respect to those in the field. As discussed in Koyama et al. (2017), there are various factors that may contribute to this discrepancy. It is likely due to different definitions for SF galaxies in our and their sample. Our SF galaxies are determined by their sSFRs while SF galaxies are detected as H_{α} galaxies in Koyama et al. (2017). In addition, it is indicated that the treatment of dust extinction or NII line contamination could easily change the results by >10 – 20% level, which can significantly ease the inconsistency between us. Finally, it is also possible that the sample size of H_{α} emitters in Koyama et al. (2017) is much smaller than that of our sample, which covers whole HSC S16A Wide survey area, and poor statistics (particularly in a high-density environment) may lead to the disagreement in conclusions.

Acknowledgments

This work is supported by the Ministry of Science & Technology of Taiwan under the grant MOST 103-2112-M-001-031-MY3 and MO is supported in part by World Premier International Research Center Initiative (WPI Initiative), MEXT, Japan, and JSPS KAKENHI Grant Number 26800093 and 15H05892. The Hyper Suprime-Cam (HSC) collaboration includes the astronomical communities of Japan and Taiwan, and Princeton University. The HSC instrumentation and software were developed by the National Astronomical Observatory of Japan (NAOJ), the Kavli Institute for the Physics and Mathematics of the Universe (Kavli IPMU), the University of Tokyo, the High Energy Accelerator Research Organization (KEK), the Academia Sinica Institute for Astronomy and Astrophysics in Taiwan (ASIAA), and Princeton University. Funding was contributed by the FIRST program from Japanese Cabinet Office, the Ministry of Education, Culture, Sports, Science and Technology (MEXT), the Japan Society for the Promotion of Science (JSPS), Japan Science and Technology Agency (JST), the Toray Science Foundation, NAOJ, Kavli IPMU, KEK, ASIAA, and Princeton University.

References

- Aihara, H., Armstrong, R., Bickerton, S., et al. (2017), arXiv:1702.08449
- Alberts, S., Pope, A., Brodwin, M., et al. 2014, MNRAS, 437, 437
- Axelrod, T., Kantor, J., Lupton, R. H., & Pierfederici, F. 2010, in Proc. SPIE, Vol. 7740, Software and Cyberinfrastructure for Astronomy, 774015
- Balogh, M. L., Navarro, J. F., & Morris, S. L. 2000, ApJ, 540, 113
- Barkhouse, W. A., Yee, H. K. C., & Lopez-Cruz, O. 2007, ApJ, 671, 1471

- Brinchmann, J., Charlot, S., White, S. D. M., et al. 2004, MNRAS, 351, 1151
- Bruzual, G., & Charlot, S. 2003, MNRAS, 344, 1000
- Butcher, H., & Oemler, A., Jr. 1984, ApJ, 285, 426
- Chabrier, G. 2003, PASP, 115, 763
- Daddi, E., Dickinson, M., Morrison, G., et al. 2007, ApJ, 670, 156
- Dressler, A., & Gunn, J. E. 1983, ApJ, 270, 7
- Dunne, L., Ivison, R. J., Maddox, S., et al. 2009, MNRAS, 394, 3
- Erfanianfar, G., Popesso, P., Finoguenov, A., et al. 2016, MNRAS, 455, 2839
- Elbaz, D., Daddi, E., Le Borgne, D., et al. 2007, A&A, 468, 33
- Elbaz, D., Dickinson, M., Hwang, H. S., et al. 2011, A&A, 533, A119
- Gerke, B. F., Newman, J. A., Faber, S. M., et al. 2007, MNRAS, 376, 1425
- Giodini, S., Finoguenov, A., Pierini, D., et al. 2012, A&A, 538, A104
- Gunn, J. E., & Gott, J. R. I. 1972, ApJ, 176, 1
- Heinis, S., Buat, V., Berthemin, M., et al. 2014, MNRAS, 437, 1268
- Ivezic, Z., Tyson, J. A., Abel, B., et al. 2008, ArXiv e-prints, arXiv:0805.2366
- Jian, H.-Y., Lin, L., Lin, K., et al. 2017, apj submitted
- Jurić, M., Kantor, J., Lim, K-T, et al. 2015, arXiv:1512.07914
- Karim, A., Schinnerer, E., Mart nez-Sansigre, A., et al. 2011, ApJ, 730, 61
- Kinney, A. L., Calzetti, D., Bohlin, R. C., et al. 1996, ApJ, 467, 38
- Koyama, Y., Smail, I., Kurk, J., et al. 2013, MNRAS, 434, 423
- Koyama, Y., et al. (2017), PASJ, In preparation
- Larson, R. B., Tinsley, B. M., & Caldwell, C. N. 1980, ApJ, 237, 692
- Li, H. I., Yee, H. K. C., & Ellingson, E. 2009, ApJ, 698, 83
- Li, H. I., Yee, H. K. C., Hsieh, B. C., et al. 2012, ApJ, 749, 150
- Lin, L., Dickinson, M., Jian, H. Y., et al. 2012, ApJ, 756, 71
- Lin, L., Koo, D. C., Weiner, B. J., et al. 2007, ApJL, 660, L51
- Lin, L., Jian, H.-Y., Foucaud, S., et al. 2014, ApJ, 782, 33
- Loh, Y.-S., Ellingson, E., Yee, H. K. C., et al. 2008, ApJ, 680, 214
- Magdis, G. E., Rigopoulou, D., Huang, J.-S., & Fazio, G. G. 2010, MNRAS, 401, 1521
- Magnier, E. A., et al. 2013, ApJS, 205, 20
- Mihos, J. C., & Hernquist, L. 1994, ApJL, 431, L9
- Mostek, N., Coil, A. L., Moustakas, J., et al. 2012, ApJ, 746, 124
- Nishizawa, A., et al. (2017), PASJ, In preparation
- Noeske, K. G., Weiner, B. J., Faber, S. M., et al. 2007, ApJL, 660, L43
- Muzzin, A., Wilson, G., Yee, H. K. C., et al. 2012, ApJ, 746, 188
- Oliver, S., Frost, M., Farrah, D., et al. 2010, MNRAS, 405, 2279
- Oguri, M. 2014, MNRAS, 444, 147
- Oguri, M., Lin, Y., Lin, S., et al. 2017, arXiv:1701.00818
- Pannella, M., Carilli, C. L., Daddi, E., et al. 2009, ApJL, 698, L116
- Peng, Y., Lilly, S. J., Kovac, K., et al. 2010, ApJ, 721, 193
- Santini, P., Fontana, A., Grazian, A., et al. 2009, A&A, 504, 751
- Schlafly, E. F., Finkbeiner, D. P., Juri, M., et al. 2012, ApJ, 756, 158
- Sobral, D., Best, P. N., Smail, I., et al. 2014, MNRAS, 437, 3516
- Speagle, J. S., Steinhardt, C. L., Capak, P. L., et al. 2014, ApJS, 214, 15
- Tanaka, M. 2015, ApJ, 801, 20
- Tonry, J. L., Stubbs, C. W., Kilic, M., et al. 2012, ApJ, 745, 42
- VALOTTO, C., MOORE, B., & LAMBAS, D. G. 2001, ApJ, 546, 157
- Wagner, C. R., Courteau, S., Brodwin, M., et al. (2017), ApJ, 834, 53
- Whitaker, K. E., van Dokkum, P. G., Brammer, G. et al. 2012, ApJL, 754, L29
- Willmer, C. N. A., Faber, S. M., Koo, D. C., et al. 2006, ApJ, 647, 853
- Zahid, H. J., Dima, G. I., Kewley, L. J., Erb, D. K., & Dave, R. 2012,